Supporting Information for

Imaging the sub-cellular viscoelastic properties of mouse oocytes

Guillaume Flé, Elijah Van Houten, Gaudeline Rémillard-Labrosse, Greg FitzHarris, Guy Cloutier

Guy Cloutier.
E-mail: guy.cloutier@umontreal.ca

This PDF file includes:

Supporting Information Text

Note 1: Advantages of NLI over other reconstruction techniques

In the first description of optical micro-elastography (1, 2), the "passive elastography" scheme was employed to recover shear stiffness distributions μ_s using a single motion component along with a purely elastic mechanical model (no damping) assuming local homogeneity, as detailed elsewhere (3–5). However, biological tissues are known to be better described as heterogeneous viscoelastic or poroelastic materials (6). Passive elastography relies on an undamped formulation of the Helmholtz wave equation, where the symmetry with respect to time is invoked to evaluate the time-reversed wave field from spatiotemporal correlations of the measured displacements across the image. The diameters of resulting focal spots relate to the approximate wavelengths λ of the elastic field according to the Rayleigh criterion. Although elegant and time efficient, this time-reversal approach is no longer valid in viscoelastic, *i.e.*, damped materials, where the material-driven attenuation of mechanical oscillations breaks the time reciprocity. Additionally, the elastic approximation $\mu_s = \rho\,(\lambda f)^2$, where f is the actuation frequency and ρ is the material's density, requires the measured elastic field be shear waves. This shear wave assumption is significantly challenged in micron and sub-micron scale confined cellular domains which restricts the reconstruction to wave parameters (λ or speed c), instead of material bio-mechanical properties, as suggested in (7). Finally, guidelines for the pre-selection of the motion component to use in the inversion procedure are rarely discussed.

The direct inversion of the algebraic wave equation has attracted a wide interest for the evaluation of the complex-valued viscoelastic shear modulus despite the required evaluation of second- to third-order displacement derivatives (8, 9). Other schemes relating measurements of wave propagation velocity and attenuation on one hand to the complex shear modulus on the other hand have also been investigated (10–12). Although reasonably simple to implement and computationally affordable, these techniques operate directly on the measured displacement field, rendering the reconstruction process prone to high sensitivity to noise. Moreover, restrictive assumptions on the wave front geometry (plane, cylindrical, spherical), wave type (pure shear versus general elastic), and tissue nature, such as local homogeneity, weaken the interpretability of final mechanical parameter estimates. The inherent heterogeneity of biological tissues and the proven pathology-driven structural changes highlight the importance of a heterogeneous mechanical parameter support (8). To date, contributions to the field of optical micro-elastography have focused on wave tracking (13) and high frequency elastic wave behaviour in gel phantoms (7), but no work has been reported on alternative characterization procedures to image the viscoelasticity in live cells.

Here, the overlapping subzone NLI approach (14) was used to recover complex-valued shear modulus distributions. Among the many options available in the literature, this choice was motivated by three criteria. First, heterogeneous property descriptions are supported as opposed to most direct strategies where property gradients are neglected to stabilize local inversions (9, 11, 15–17). Second, the low compressibility found in most biological tissues (18) is handled by the introduction of both an additional equation and a pressure term as in (19). This approach is distinguished from the more common isolation of the elastic field's compression component through extensive spatial filtering or formal extraction of the shear component, at the cost of high-order differentiation of the noisy displacement data. Finally, complex elastic fields of relatively large wavelengths (on the order of the domain scale), similarly to that generated under the available actuation frequency in optical micro-elastography, cannot be associated to simple shear waves and have been shown to depend on mechanical properties and domain geometry, thus requiring explicit integration of boundary condition information in the reconstruction process (7). In NLI, the generalized boundary value problem does not assume the presence of bulk shear waves. Numerical simulations of the boundary value problem are computed iteratively using successive sets of material property updates until the simulated displacements match the measured displacements in a least-squared sense. Boundary conditions are thus supplied to the forward finite element algorithm under the form of displacement values extracted from the actual measured data. Fig. S1 shows micro-elastography reconstructions from previous (using the same data set as (1)) and presented works. The attenuation-free shear stiffness map from previous work has been converted back to speed values, *i.e.*, $c = \sqrt{\mu_s/\rho}$, due to the violation of the shear wave assumption (7). For comparison, the transparency map in previous work has been removed and anatomical and property images are displayed side-by-side instead of superimposed. The shear stiffness computed with NLI is defined by $\mu_s = 2\frac{|\mu_r+i\mu_i|^2}{\mu_r+|\mu_r+i\mu_i|}$, where μ_r and μ_i are the reconstructed storage and loss moduli, respectively. The presented micro-elastography pipeline results in more detailed property maps where individual regions (nucleolus, nucleus, cytoplasm, perivitelline space, and zona pellucida) are clearly outlined and distinguishable.

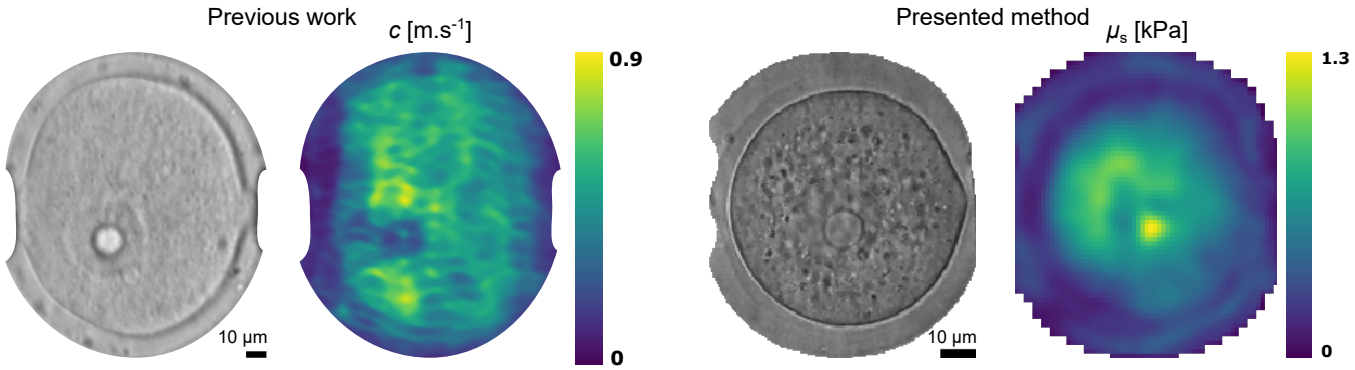

Fig. S1. Micro-elastography reconstructions from previous (1) and presented works. c is the speed of the elastic wave satisfying the wave propagation equation, and μ_s is the shear stiffness of the oocyte.

Note 2: Full-field displacement approximation

The rationale for full-field displacement data approximation from in-plane measurements is described in this section. GV-stage oocytes have been commonly described as symmetrical cells. This characteristic, combined with an in-plane actuation at the central symmetry level of the oocyte, allows to infer the motion component variations in the vicinity of this central slice. A 3D oocyte displacement model was built to demonstrate the assumptions underlying the approximation of full-field displacements. Fig S2 shows the variations of motion component amplitudes $|u|$, $|v|$, and $|w|$ averaged in (x, y) planes along the z axis in the upper-half ($z = 0$ µm to $z = 45$ µm) of a simulated 3D oocyte domain. The slice located at $z = 0$ µm is the plane of symmetry of the oocyte model and motion components u, v, and w are oriented along the x, y, and z axes, respectively.

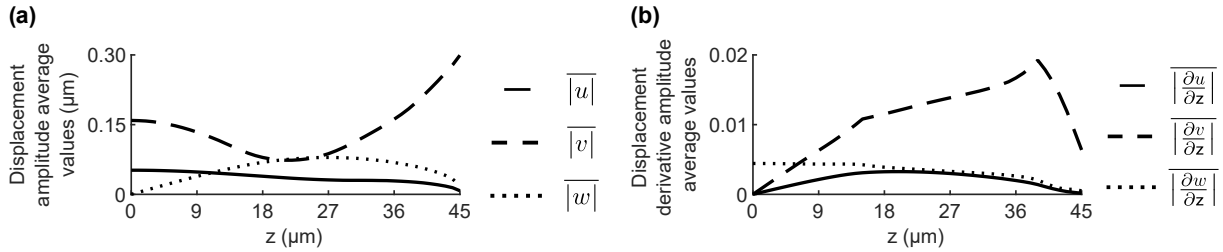

Fig. S2. Variations along the z axis of motion component amplitude average values.

In Fig. S2.a, components $\overline{|u|}$ and $\overline{|v|}$ are non-zero at every slice location along the z axis, whereas $\overline{|w|}$ is zero in the central plane and progressively increases. This indicates the following motion variations:

$$\begin{cases} w = 0 & \text{if } z = 0, \\ w \neq 0 & \text{if } z \neq 0, \\ u \neq 0 & \forall z, \\ v \neq 0 & \forall z. \end{cases} \quad [1]$$

In Fig. S2.b, $\overline{\left|\frac{\partial u}{\partial z}\right|}$ and $\overline{\left|\frac{\partial v}{\partial z}\right|}$ are zero or small in the central plane and its vicinity, respectively, and grow at increased distances from $z = 0$ µm. On the contrary, $\overline{\left|\frac{\partial w}{\partial z}\right|}$ is non-zero at $z = 0$ µm and progressively decreases. This indicates the following motion variations:

$$u_{z_0} \approx u_{z_0+\delta z}, \quad [2]$$
$$v_{z_0} \approx v_{z_0+\delta z}, \quad [3]$$
$$w_{z_0} \neq w_{z_0+\delta z}, \quad [4]$$

where $z_0 = 0$ µm. These observations support the effort for displacement recovery in the neighborhood of the measured central plane. In particular, the incompressibility of biological tissues (18) enables the approximation of the out-of-plane component w through $\nabla \cdot \mathbf{u} = 0$ (local incompressibility), which represents an alternative to the more common approach of invoking plane-strain when tomographic data are measured.

Note 3: Experiment-based full and partial convergence rates from two representative oocytes

Two typical convergence profiles were observed in the presented work and are shown in Fig. S3 through two representative oocytes. The storage modulus reconstructions performed on the 21 treated oocytes all converged to a stable distribution (μ_r curves for the representative oocytes 1 and 2 in Fig. S3). Out of the 21 corresponding loss modulus reconstructions, 13 converged to a stable distribution (plateau in the convergence profile of the representative oocyte 1 for μ_i) and 8 continued to progress towards lower values (slope in the convergence profile of the representative oocyte 2 for μ_i). In general, the loss modulus is responsible for subtle variations in the shape of the induced wave field and is more difficult to identify, especially when the wavelength is long, than the storage modulus, which is most responsible for this wavelength. This explains the overall higher sensitivity of the algorithm to storage than loss modulus contrasts.

The partial convergence observed here suggests that the algorithm has identified a relative distribution of loss modulus values and pursues the reconstruction by promoting property updates that lead to a global scaling with additional iterations. This is shown in Figs. 3.e and 3.f in the article, where the map of the partially-converged loss modulus is consistent with its fully-converged counterpart but shows lower magnitude values and spatial variations of lower definition.

This characteristics might be indicative of a natural biological variability where the elastic wave attenuating behavior of some oocytes might be slightly lower than in others, and which would translate into attenuation effects even harder to detect in the measured wave field. Although the oocytes in question would remain fully viscoelastic in terms of the elastic versus viscous contribution, slightly lower loss modulus values in this already low and narrow range (within a few hundreds of Pascals) might have hindered the generation of a quantitative property update.

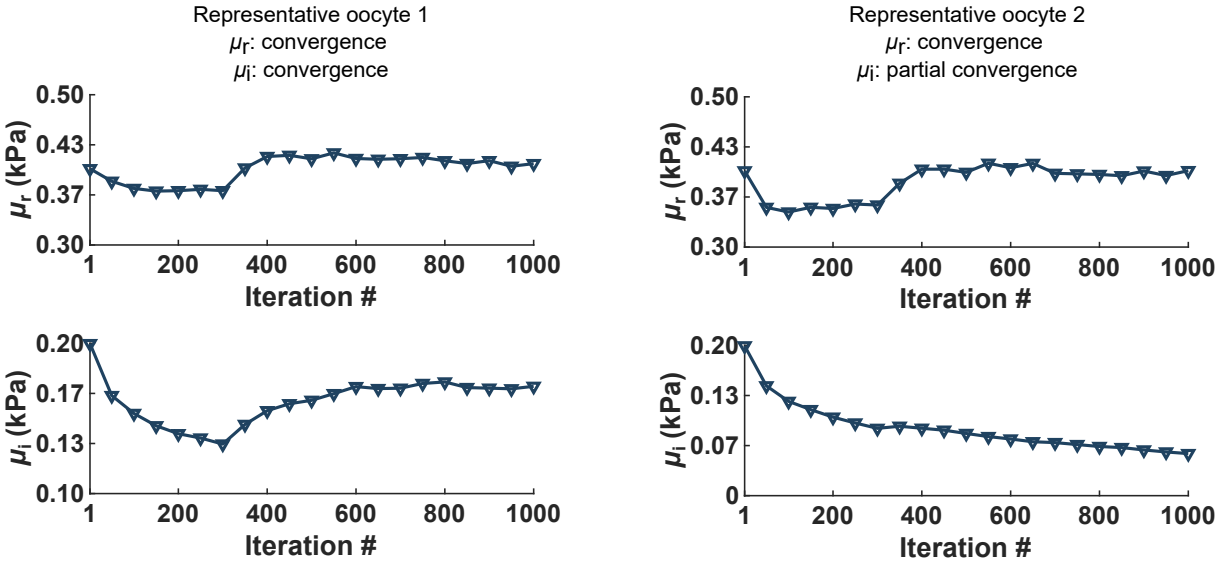

Fig. S3. Full and partial convergence rates from two representative oocytes.

Note 4: Reconstructions from true full-field displacements

The proposed method introduces an important advance in the field of optical micro-elastography. However, future work involving metaphase-II stage oocytes and early fertilized embryos in the context of *in-vitro* fertilization will require the measurement of actual true volume data to leverage the full potential of the proposed pipeline, and extend its applicability to cells of arbitrary shapes. Fig. S4 shows maps of relative reconstruction errors when the true 14.4-kHz full-field displacements simulated in the oocyte model, with the shear modulus distributions μ_1 and μ_2 described in the article, are used for inversion. Storage modulus reconstructions with reasonable to numerical precision accuracy could be recovered from both μ_1 and μ_2 displacement data, the loss modulus reconstructed from μ_2 displacement data also presented a reasonable accuracy, and the loss modulus reconstructed from μ_1 displacement data showed the highest error levels, which was expected due to the long wavelength of the induced vibrations.

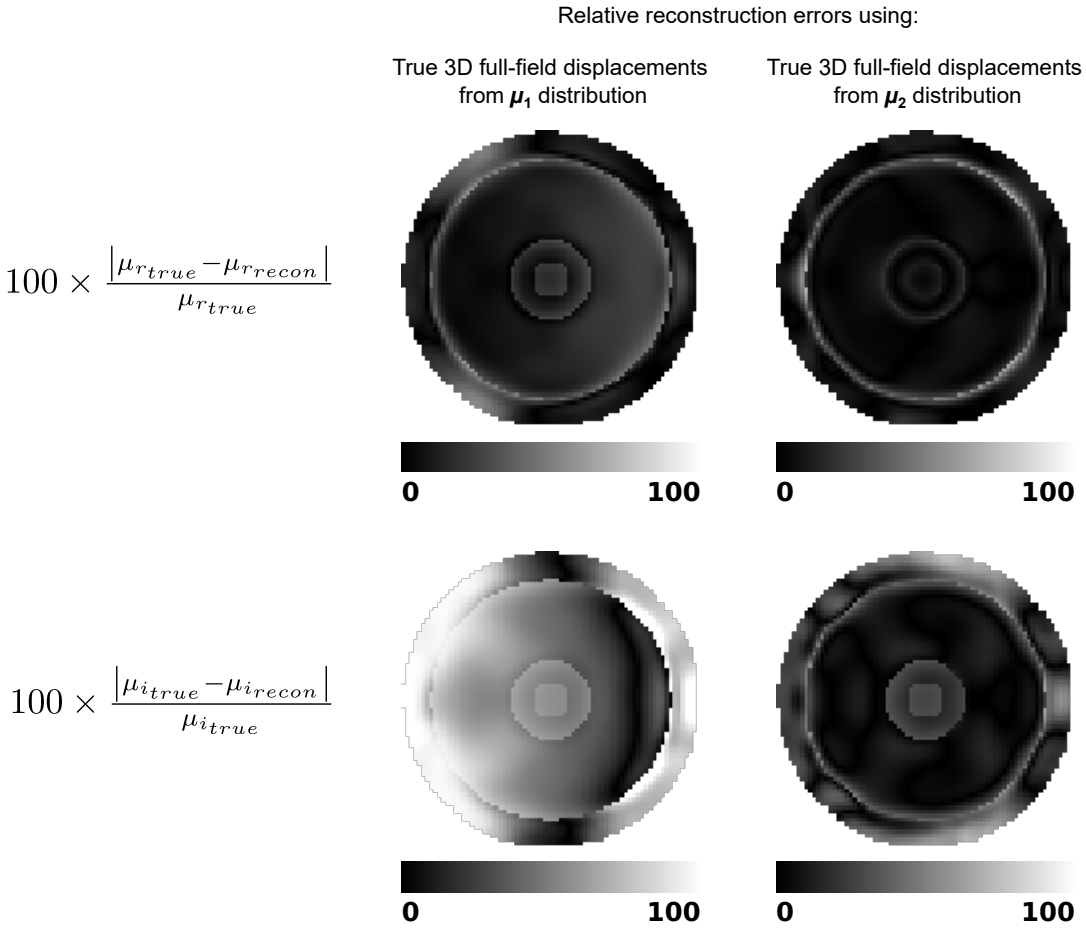

Fig. S4. Maps of the NLI reconstruction errors using simulated true 3D full-field displacements.

Note 5: Selection of the zone size and inter-slice distance

The division of the total region of interest into a collection of subzones randomly distributed permits to handle the reconstruction and its computational cost, irrespective of the mechanical property's potential spatial variations, which cannot always be anticipated. Nevertheless, constraints are placed on the size of those subzones relatively to the wavelength of the measured wave field, which is governed by the mechanical properties of the scanned tissue and the actuation frequency. Once the subzone size is fixed, no constraint is placed on the storage and loss modulus relative spatial variations, *i.e.*, the algorithm identifies the property updates freely.

Previous works have demonstrated that the subzone size plays an important role in the reconstruction process and that mechanical contrasts in the imaged material could be recovered from the collected motion fields with subzone size to wavelength ratios of various extents (20–23). In particular, experimental conditions involving different wavelengths were investigated and allowed establishing guidelines to resolve property distributions in the material. However, these guidelines were established using true 3D-displacement data acquired with magnetic resonance elastography.

In our work, 2D displacements were estimated from optical microscopy images and expanded to an approximated 3D data set using an oocyte geometry-based 3D mechanical motion model. This step introduced an additional parameter to optimize (the inter-slice distance), which, together with the subzone size, were found to be competing reconstruction variables in the present situation where elastic fields of long wavelengths were induced. Consequently, guidelines adapted to our experimental conditions were proposed by studying these two parameters and their joint impact on the recovered property maps.

In practice, inversion configurations allowing stable reconstructions while minimizing the computational needs are preferred. A stability study was conducted in this respect to identify a suitable subzone size - inter-slice distance combination. Five inter-slice distances ranging from $\delta z_1 = 0.25$ µm to $\delta z_5 = 1.25$ µm were used to assess the impact of the local approximation discretization, which remains valid in the vicinity of the central plane, along with three subzone isotropic sizes, $zs_1 = 20$ µm, $zs_2 = 30$ µm, and $zs_3 = 40$ µm. Zone sizes smaller than 20 µm would cover less than 25 % of the wavelength, which would further challenge the reconstruction, and sizes greater than 40 µm would be inconsistent with the advantages of the subzone decomposition.

Fig. S5.a shows reconstructions of the storage modulus with the five inter-slice distances and three zone sizes. Fig. S5.b shows the corresponding reconstructions of the loss modulus. The property images indicate that the computation of the inverse problem performed better with a larger discretization of the local divergence-free approximation, as the smallest inter-slice distance ($\delta z_1 = 0.25$ µm) resulted in the poorest contrast quality between inner structures of the representative oocyte. The different scales observed in the estimated properties, alongside zone size variations, are consistent with reconstruction behaviours reported in low frequency and intrinsic MR elastography, where the low-frequency, long-wavelength condition precludes absolute property recovery (23). The right panels of Fig. S5.a and S5.b display the convergence rates of the iterative reconstructions indicated by the average value of the property across the entire domain.

In this context of optical micro-elastography, the selection of the optimal inter-slice distance and zone-size was addressed by evaluating the relative variations of the recovered properties with respect to each parameter using finite-difference derivatives, *i.e.*, $\overline{\left|\frac{\partial\theta}{\partial zs}\right|}/\sigma_\theta$ and $\overline{\left|\frac{\partial\theta}{\partial\delta z}\right|}/\sigma_\theta$, where θ represents the storage (μ_r) or loss (μ_i) modulus. Fig. S6 shows these relative variations for each combination of inter-slice distance and subzone size. The optimal configuration was identified by the minimum values of $\overline{\left|\frac{\partial\theta}{\partial zs}\right|}/\sigma_\theta$ and $\overline{\left|\frac{\partial\theta}{\partial\delta z}\right|}/\sigma_\theta$ shared by μ_r and μ_i. Reconstructions involving δz_1 and δz_2 were discarded due to their poor convergence rates, as indicated in Fig. S6. Amongst the remaining parameters, δz_3 to δz_5 and zs_1 to zs_3, a shared minimum was found for the ($\delta z_5 = 1.25$ µm, $zs_2 = 30$ µm) combination.

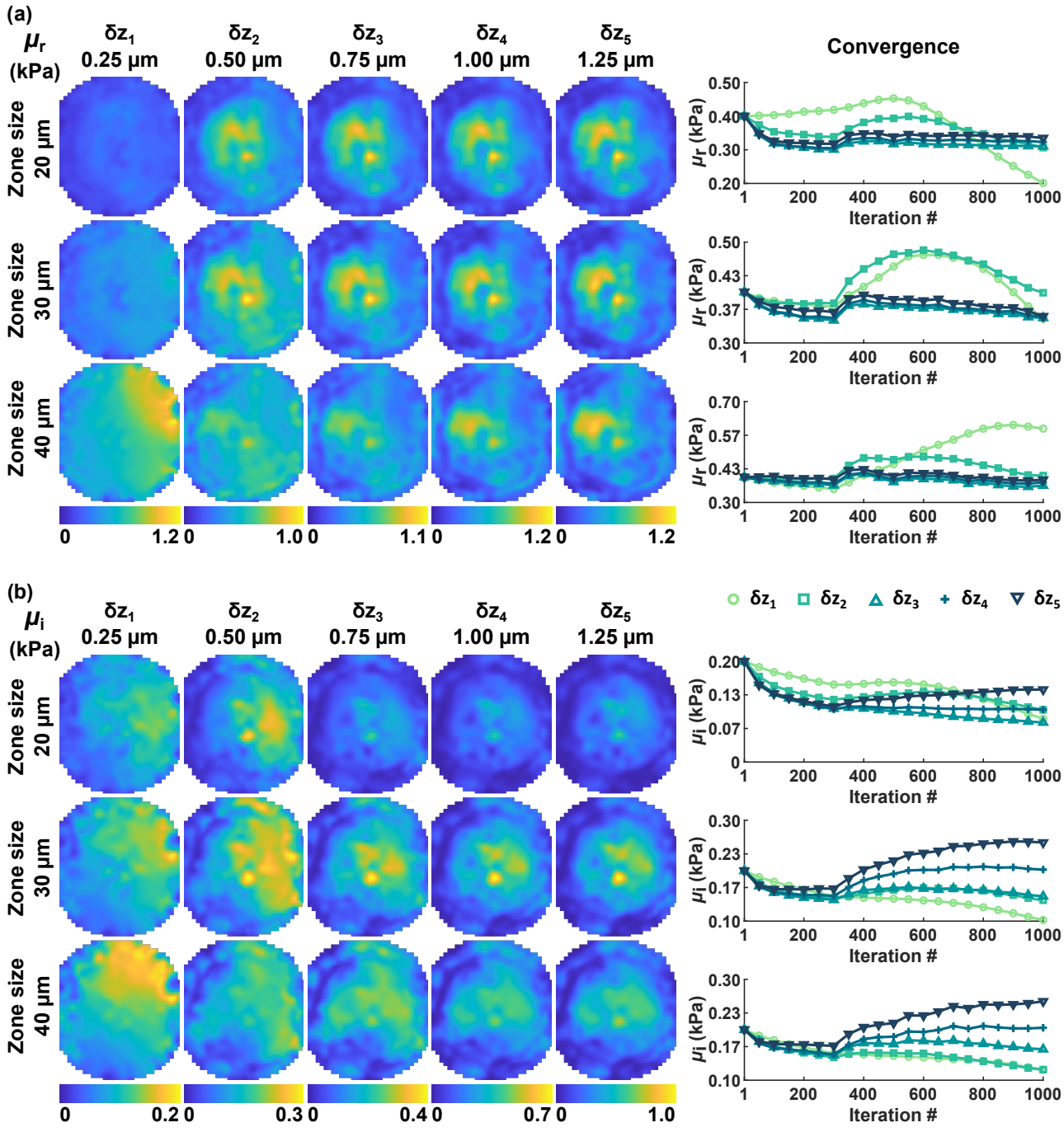

Fig. S5. Impact of the inter-slice distance δz and of the zone size zs on the recovered property images.

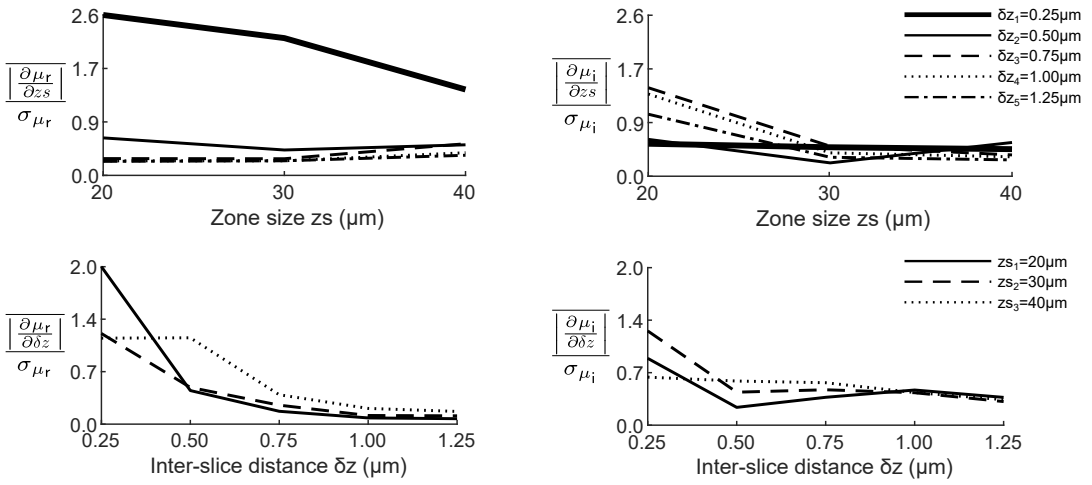

Fig. S6. Selection of the optimal inter-slice distance and zone-size. The relative variations of the reconstructed properties are reported in percentage of the property's standard deviation calculated in each segment (nucleolus, nucleus, cytoplasm, perivitelline space, and zona pellucida) and averaged across all segments.

References

1. P Grasland-Mongrain, et al., Ultrafast imaging of cell elasticity with optical microelastography. *Proc. Natl. Acad. Sci.* **115**, 861–866 (2018).
2. JP Kraack, Biophysics: Ultrarapid microquakes. *Res. Highlights, Nat. Phys.* **14**, 206–206 (2018).
3. J Brum, S Catheline, N Benech, C Negreira, Quantitative shear elasticity imaging from a complex elastic wavefield in soft solids with application to passive elastography. *IEEE Transactions on Ultrason. Ferroelectr. Freq. Control.* **62**, 673–685 (2015).
4. T Gallot, et al., Passive elastography: Shear-wave tomography from physiological-noise correlation in soft tissues. *IEEE Transactions on Ultrason. Ferroelectr. Freq. Control.* **58**, 1122–1126 (2011).
5. J Brum, N Benech, T Gallot, C Negreira, Shear wave elastography based on noise correlation and time reversal. *Front. Phys.* **9**, 617445.1–9 (2021).
6. PR Perrinez, FE Kennedy, EEWV Houten, JB Weaver, KD Paulsen, Modeling of soft poroelastic tissue in time-harmonic mr elastography. *IEEE Transactions on Biomed. Eng.* **56**, 598–608 (2009).
7. G Laloy-Borgna, A Zorgani, S Catheline, Micro-elastography: Toward ultrasonic shear waves in soft solids. *Appl. Phys. Lett.* **118**, 113701.1–6 (2021).
8. H Li, et al., Viscoelasticity imaging of biological tissues and single cells using shear wave propagation. *Front. Phys.* **9**, 66–103 (2021).
9. R Sinkus, et al., Viscoelastic shear properties of in vivo breast lesions measured by mr elastography. *Magn. Reson. Imaging* **23**, 159–165 (2005).
10. M Bhatt, et al., Reconstruction of viscosity maps in ultrasound shear wave elastography. *IEEE Transactions on Ultrason. Ferroelectr. Freq. Control.* **66**, 1065–1078 (2019).
11. H Knutsson, C Westin, G Granlund, Local multiscale frequency and bandwidth estimation in *Proceedings of 1st International Conference on Image Processing.* (IEEE Computer Society), Vol. 1, pp. 36–40 (1994).
12. S Bernard, S Kazemirad, G Cloutier, A frequency-shift method to measure shear-wave attenuation in soft tissues. *IEEE Transactions on Ultrason. Ferroelectr. Freq. Control.* **64**, 514–524 (2017).
13. A Zorgani, TA Ghafour, M Lescanne, S Catheline, A Bel-Brunon, Optical elastography: Tracking surface waves with digital image correlation. *Phys. Medicine Biol.* **64**, 055007.1–9 (2019).
14. EEW Van Houten, KD Paulsen, MI Miga, FE Kennedy, JB Weaver, An overlapping subzone technique for mr-based elastic property reconstruction. *Magn. Reson. Medicine* **42**, 779–786 (1999).
15. EH Clayton, JR Garbow, PV Bayly, Frequency-dependent viscoelastic parameters of mouse brain tissue estimated by mr elastography. *Phys. Medicine Biol.* **56**, 2391–2406 (2011).
16. TE Oliphant, A Manduca, RL Ehman, JF Greenleaf, Complex-valued stiffness reconstruction for magnetic resonance elastography by algebraic inversion of the differential equation. *Magn. Reson. Medicine* **45**, 299–310 (2001).
17. A Manduca, R Muthupillai, PJ Rossman, JF Greenleaf, RL Ehman, Local wavelength estimation for magnetic resonance elastography in *Proceedings of 3rd IEEE International Conference on Image Processing.* (IEEE), Vol. 3, pp. 527–530 (1996).
18. AP Sarvazyan, OV Rudenko, SD Swanson, JB Fowlkes, SY Emelianov, Shear wave elasticity imaging: A new ultrasonic technology of medical diagnostics. *Ultrasound Medicine Biol.* **24**, 1419–1435 (1998).
19. L Tan, et al., Gradient-based optimization for poroelastic and viscoelastic mr elastography. *Transactions on Med. Imaging* **36**, 236–250 (2017).
20. AT Anderson, et al., Inversion parameters based on convergence and error metrics for nonlinear inversion mr elastography in *Proc. intl. soc. mag. reson. med.* Vol. 25, p. 1139 (2017).
21. LM Solamen, MD McGarry, L Tan, JB Weaver, KD Paulsen, Phantom evaluations of nonlinear inversion mr elastography. *Phys. Medicine Biol.* **63**, 145021.1–14 (2018).
22. SW Gordon-Wylie, et al., Mr elastography at 1 hz of gelatin phantoms using 3d or 4d acquisition. *J. Magn. Reson.* **296**, 112–120 (2018).
23. M McGarry, et al., Uniqueness of poroelastic and viscoelastic nonlinear inversion mr elastography at low frequencies. *Phys. Medicine Biol.* **64**, 075006.1–14 (2019).